Effect of flue gas composition on deposit induced high temperature corrosion under laboratory conditions mimicking biomass firing. Part II: Exposures in SO2 containing atmospheres

Okoro, Sunday Chukwudi; Kiamehr, Saeed; Montgomery, Melanie; Jappe Frandsen, Flemming; Pantleon, Karen

Published in:
Materials and Corrosion

Link to article, DOI:
10.1002/maco.201609174

Publication date:
2017

Document Version
Peer reviewed version

Effect of flue gas composition on deposit induced high temperature corrosion under laboratory conditions mimicking biomass firing. Part II: Exposures in SO_2 containing atmospheres

Sunday Chukwudi Okoro[1,*], Saeed Kiamehr[1], Melanie Montgomery[1], Flemming Jappe Frandsen[2], Karen Pantleon[1]

[1] Department of Mechanical Engineering, Technical University of Denmark (DTU), 2800 Kongens Lyngby, Denmark.

[2]CHEC Research Centre, Department of Chemical and Biochemical Engineering, DTU, 2800 Kongens Lyngby, Denmark.

* Phone: +45 50185680, Fax: +45 45936213, Email: sunoko@mek.dtu.dk, okorochukwudi@ymail.com

Abstract

In biomass fired power plants, the fast corrosion of superheaters is facilitated by the presence of corrosive flue gas species, for example, SO_2 , which are released during combustion. To understand the role of the gas species on the corrosion process, comparative laboratory exposures of deposit (KCl)-coated and deposit-free austenitic stainless steel (TP 347H FG) samples to gas mixtures containing SO_2 was carried out, under conditions relevant to biomass-firing. Exposures were conducted isothermally at 560 ^oC for 72 h, in oxidizing-sulphidizing, and oxidizing-sulphidizing-chlorinating gas mixtures containing 60 ppmv SO_2. Scanning Electron Microscopy (SEM), Energy dispersive X-ray spectroscopy (EDS) and X-ray diffraction (XRD) techniques were complimentarily applied to characterize the resulting corrosion products. A partially molten K_2SO_4-layer formed on KCl coated specimens, and corrosion resulted in localized broad pits containing sulphides and oxides. The severe pitting attack was decreased by the presence of HCl in the gas mixture.

Keywords: High temperature corrosion, Stainless steel, Sulphation, Chlorination, Sulphidization, Metal chlorides.

1. Introduction

Although current environmental awareness calls for a shift towards greener energy sources, combustion of biomass (especially straw) in power plants is still challenging due to various operational difficulties such as slagging and fouling, and corrosion in the boiler [1,2]. This is because the chemical composition of biomass-based fuels differs considerably from that of fossil fuels, resulting in much higher corrosion rates [3]. Typically, biomass-based fuels contain high contents of potassium (K) and chlorine (Cl) [4] and during combustion, release of these species leads to deposition of alkali chloride-rich deposits on superheaters [2]. Prompted by this challenge, a number of investigations have focused on studies related to KCl-induced corrosion of superheater materials (see for example [5–9]). Generally, investigations have revealed that both the alkali metal cation and chloride anion participate in the fast corrosion of investigated alloys. Specifically, the alkali metal cation, potassium, has been reported to play the crucial role in disrupting the formation of protective chromium-rich oxide during the initiation stages of corrosion attack [5,8,10]. These results are based on studies under fairly oxidizing conditions with gas mixtures comprising of oxygen (O_2) and water (H_2O) vapour. However, results from full-scale investigations [3,11,12] have shown the presence of sulphur containing corrosion products in addition to KCl and oxides of the alloying elements. Such observations emphasize the importance of including other gaseous species in laboratory investigations to enable a closer simulation of conditions in the boiler.

Organically or inorganically bound sulphur in the fuel is also released as sulphur (IV) oxide (SO_2) during combustion, in the devolatilization and char combustion stages [2,13,14]. The concentration of SO_2 in the flue gas can influence both the formation of deposits and corrosion of superheaters. It is reported that SO_2 can react in the gas phase with potassium chloride (KCl) vapour to form potassium sulphate (K_2SO_4) nuclei for further condensation of KCl [2,15]. Despite its importance, the role of SO_2 with respect to corrosion of superheaters under biomass-firing conditions is still not fully understood. Studies have shown that conversion of KCl to K_2SO_4 due to the presence of SO_2 in the gas reduces the corrosion attack [16–18]. This was justified on the basis that K_2SO_4 has lesser tendency to cause formation of potassium chromate (K_2CrO_4) and therefore will not prevent formation of the protective chromia (Cr_2O_3) scale. However, it has to be noted that in some of these studies [17,19], (probably) due to the formation of hydrogen chloride (HCl) from the conversion of KCl to K_2SO_4, a higher mass gain of samples was recorded than that observed while using only K_2SO_4 as deposits. Some studies [2,3,20] have attributed the ability of (H)Cl generated from the sulphation of alkali chloride deposits to induce cyclic chlorination of alloying elements, as the major process responsible for corrosion of superheaters. However, it has been pointed out that the concentration of SO_2 employed for corrosion studies using alkali chloride deposits may influence the effect of the resulting HCl on corrosion. Specifically, while using as high as 15000 ppm of SO_2 [21], it was suggested that the observed reduction in corrosion attack was due to preferential sulphation of deposit particles at the gas/deposit interface leading to reduced generation of HCl close to the deposit/alloy interface. This therefore implies that depending on its concentration, SO_2 may exert a positive or negative effect on corrosion attack. Based on results from full-scale flue gas measurements in power plants firing biomass, the maximum SO_2-concentration

measured before the superheater section as well as in the stack, was below 120 ppm [12,22–24]. In addition, the composition of the flue gas is not strictly oxidizing as has been employed in most laboratory investigations addressing the effect of SO_2. Therefore it is important to investigate the influence of SO_2 on corrosion of superheaters, under gas mixtures similar to biomass boiler conditions in order to understand the related corrosion mechanisms under such conditions.

This paper is the second part of the study addressing the effect of flue gas composition on the corrosion of superheaters in biomass-fired boilers using laboratory scaled investigations. Part I [25] reports on the effect of Cl containing species (in both the deposit and the gas phase) on the corrosion of a superheater material (TP 347H FG). The present paper (Part-II) focusses on the influence of SO_2 in the gas phase during corrosion of the same superheater material. In analogy to part-I of this study [25], the present investigation considers both deposit-free and KCl-deposited samples, and it also addresses the influence of additional HCl in the gas phase, to clarify the effect of the interaction between SO_2 and deposit particles on corrosion.

2 Experimental

2.1 High temperature corrosion exposure

An austenitic stainless steel (TP 347H FG) tube with the following chemical composition was used for the experiments: 18.1 wt% chromium (Cr), 10.3 wt% nickel (Ni), 2.0 wt% manganese (Mn), 0.5 wt% niobium (Nb), 0.4 wt% silicon (Si) with iron (Fe) as balance. According to [26], the alloy has a carbon content of 0.057 wt%. From the tube, rings with a width of 10 mm (longitudinal direction of the tube) were cut and further segmented such that arc shaped samples with arc length of 14.6 mm were obtained. The wall thickness of the tube, i.e. the height of the samples, was 7.4 mm. Prior to corrosion exposures, the samples were cleaned by ultrasonically degreasing in acetone followed by drying in ethanol. Afterwards, samples to be exposed with a deposit were coated with a slurry of the synthetic KCl deposit which was obtained by dispersing 32 – 63 µm sized KCl particles (Sigma, $\geq$ 99%) in a solution of 2-propanol. Using deposit slurries to coat samples provides a means of obtaining a tight contact between deposit particles and the sample surface, so as to closely mimick the conditions in real superheaters. A final thickness of the KCl-deposit of 1 mm was obtained after drying the coating on the sample. Samples for exposures under deposit-free conditions were directly exposed in the as-cleaned state.

The corrosion test rig utilised is shown in Figure 1 and consists of a gas mixing unit, an electrically heated furnace and a scrubber system for cleaning the flue gas. Using mass flow controllers in the gas mixing unit, the desired concentration of each gas component was obtained. To incorporate 13.4 vol % of water vapour (H_2O) in the gas stream, the carrier gas (nitrogen - N_2), carbon (IV) oxide (CO_2) and oxygen (O_2) were all bubbled through a water flask maintained at 52 ^oC. The final gas stream comprised of a mixture of the humid oxidizing gas (H_2O, CO_2 and O_2), SO_2 (and HCl) which was fed into the reactor through a preheated gas channel to avoid condensation. The total gas flow rate in the inlet stream was 1000 $mLmin^{-1}$.

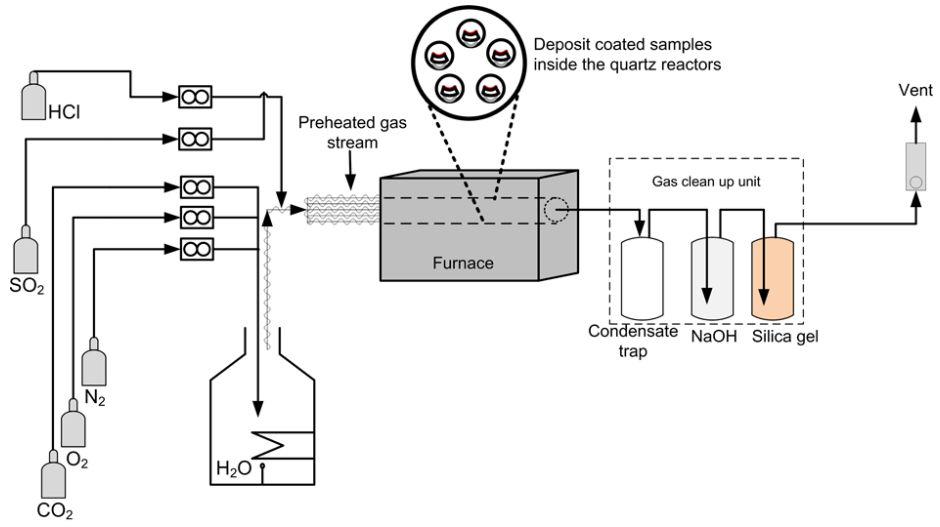

Figure 1. Schematic representation of the corrosion test rig employed for the high-temperature exposures.

Table 1 summarizes the four different exposures considered in the present study. Under both oxidizing-sulphidizing and oxidizing-sulphidizing-chlorinating gas mixtures, deposit-coated and deposit-free samples were exposed. The oxidizing-sulphidizing-chlorinating gas mixture mimics the condition during straw-firing [27] where the HCl concentration is chosen to reflect the worst case situation . Each experimental condition involved a minimum of 4 samples placed in quartz reactors inside the furnace in positions parallel to the direction of gas flow. Exposures were carried out isothermally at 560 ^{o}C for 72 h after which samples were allowed to cool inside the reactors under a flow of N_2**.**

Table 1. A summary of the experimental conditions investigated in the present study.

Experiment	Deposit coated?	Gas composition
IIIa	Yes	Oxidizing-sulphidizing gas: SO_2 – 60 ppmv (dry), O_2 – 6 vol % (dry), CO_2 – 12 vol % (dry), N_2 – 82 vol % (dry) and H_2O – 13.4 vol %
IIIb	No	
IVa	Yes	Oxidizing-sulphidizing-chlorinating gas: HCl – 400 ppmv (dry), SO_2 – 60 ppmv (dry), O_2 – 6 vol % (dry), CO_2 – 12 vol % (dry), N_2 – 82 vol % (dry) and H_2O – 13.4 vol %
IVb	No	

2.2 Corrosion product characterization

For comprehensive characterization of the corrosion products, both cross-sectional and the plan 'top-down' approaches [7] were employed. This involved the complementary use of scanning electron microscopy (SEM), energy dispersive spectroscopy (EDS) and X-ray diffraction (XRD). For cross-sectional characterization of corrosion products, samples were mounted in epoxy under vacuum using a two-stage process (for details of metallographic preparation, see [7]).

In the plan view 'top-down' approach, characterization was undertaken directly on surfaces of exposed samples and continued on the successively revealed surfaces after several steps of mechanical removal of the corrosion products with a scalpel or silicon carbide (SiC) paper. This stepwise removal and characterization of exposed surface reveals detailed information that supplements microstructure information obtained from cross-sections. A detailed explanation of this approach in addition to its advantages for characterization of corrosion products is given elsewhere [7].

An Inspect S (FEI instruments) microscope was used for SEM investigations on both cross-sections and plan views. An acceleration voltage of 15 keV was used and imaging was carried out using the backscatter electron detector (BSE) unless otherwise stated. EDS was also carried out in the SEM using an acceleration voltage of 15 keV to determine the chemical composition of the corrosion products. Both Aztec and Inca (Oxford instruments) software were used for EDS analysis. EDS results presented here are limited to concentrations above 1 wt % which are representative for the otherwise heterogeneous corrosion products. For qualitative phase analysis, XRD was carried out as part of the plan view 'top-down' characterization, thus, on both the original surfaces and after successive mechanical removal of the corrosion product layers. A Bruker AXS (D8 Discover) diffractometer equipped with a Cr Kα radiation source was used in grazing incidence geometry (GI-XRD, grazing incidence angle, $\gamma = 2^{o}$), whereby the X-ray penetration depth was confined to thicknesses lower than that of the removed layer in each case. However in the case of deposit-free samples involving no further removal of the thin corrosion products, the incidence angle (γ) was raised to 5^{o} to increase the X-ray penetration depth and probe more sample volume. Due to the curved geometry of the samples, the incident beam was converged using a polycap optic system into a point focused beam.

In addition to experimental investigations, thermodynamic calculations were performed with FactSage 7.0 [28,29] using the FactPS, FT oxid, FT salt, and FT pulp databases. The calculations were used to support some of the experimental findings and were based on minimizing the Gibbs free energy of the systems considered.

3. Results

3.1 KCl-coated samples exposed to an oxidizing-sulphidizing gas (Experiment IIIa)

From examinations of cross-sectioned deposit-coated samples exposed to the oxidizing-sulphidizing gas mixture (experimental condition IIIa), two different types of corrosion product morphologies were observed (Figure 2a and b). In some areas the corrosion product appears rather homogeneous in thickness with flat topography (Figure 2a), whereas in other regions there is a dome-like appearance (Figure 2b) with corresponding extensive pitting of the alloy.

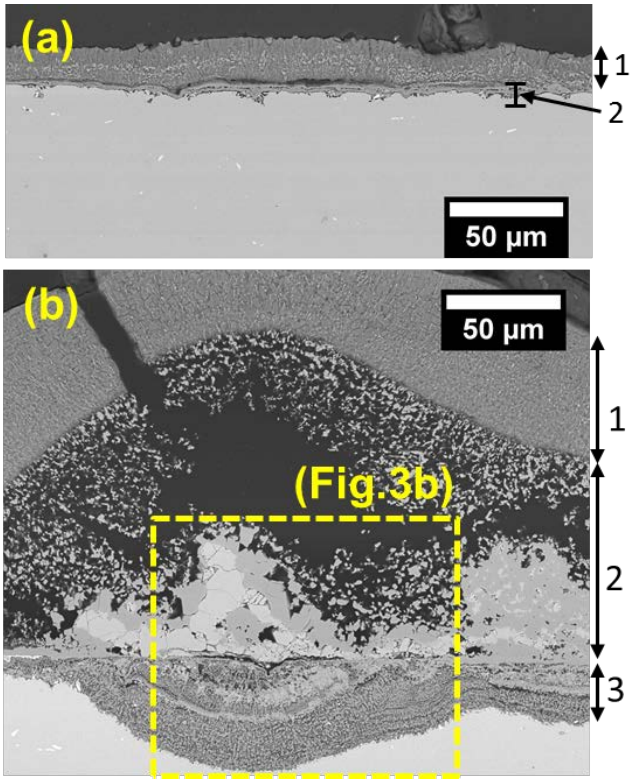

Figure 2. Cross-section of corrosion products showing (a) regions with flat morphology and (b) regions with pitting morphology after exposure of KCl-coated samples to an oxidizing-sulphidizing gas mixture (experiment IIIa). The different types of morphologies in (a) and (b) were equally distributed across the sample cross section. Double-headed arrows 1–3 indicate the different layers of corrosion product. Note that the deposits are not visible in both micrographs.

The different types of morphologies were distributed equally across the sample cross section, thus none of the morphology types was predominant. The corrosion product layers identified in regions comprising each of these morphologies are indicated by double-headed arrows (1-3) in Figure 2. As revealed by the contrast in the micrographs (Figure 2), layer 1 of the corrosion product was present in both types of morphology and is apparently a mixture of two phases. For regions with the flat morphology, layer 2 was a relatively compact layer while in regions with the dome-like appearance; layer 2 consisted of finely

dispersed particles located closer to layer 1, and a mixture of two phases located above the assumed original sample surface. Layer 3 exists as broad pits below the “original” metal surface and was only present in regions with dome-like appearance.

Elemental distribution maps in Figure 3a show that layer 1in Figure 2a, contains Fe, Mn, K, S, and O. The relatively compact layer 2 in regions with flat morphology (Figure 2a) is revealed by the EDS maps in Figure 3a to contain Fe, Cr and O, with a band of S in the lower part. Local regions enriched in Ni were also present at the interface between layer 2 and the alloy bulk. For regions with pitting attack, the elemental composition of layer 1 was similar with that of layer 1 in Figure 3a, and hence, not repeated here. EDS maps in Figure 3b show that for the regions with pitting attack, the dispersed particles located closer to layer 1 were Fe and O rich. However, the mixture of two phases located above the assumed original sample surface (Figure 2b) are Fe-O rich (darker regions) and Ni-S rich (brighter regions) as revealed by EDS maps in Figure 3b. The broad pits below the “original” metal surface (i.e. layer 3 in Figure 2b) consist of Fe, Cr, S and O (Figure 3b). A Ni enriched band is formed within the alloy adjacent the corrosion front and on some locations, this layer was porous (Figure S1, supporting information).

Plan view investigations on the deposit after the exposure showed the accumulation of faceted particles on the deposit particles (Figure 4a, b), which was not visible in the cross-sections. These accumulations were present both at the gas/deposit and deposit/corrosion product interfaces, but the faceted particles were smaller at the latter interface (Figure 4b). At the gas/deposit interface, EDS analysis showed the faceted particles to consist of K, S and O with the following concentration (wt %): K–41.7, S-18.4 and O–39.9. However, the original deposit particles were not completely covered with the faceted particles at the deposit/corrosion product interface, and therefore EDS analysis showed the presence of about 2.2 wt % Cl.

A secondary electron (SE) plan view micrograph is shown in Figure 4c revealing both flat and dome-like morphologies, beneath the deposit (corresponding to layer 1 in the cross-sections). A close-up BSE micrograph of regions with flat morphology (Figure 4d) gives the appearance of a molten phase with small particles of another composition. Similar to the result from the cross section, EDS analysis showed the presence of (in wt %): Fe–1.9, Mn–6.6, K–38.4, S–16.8 and O–36.3 in this layer.

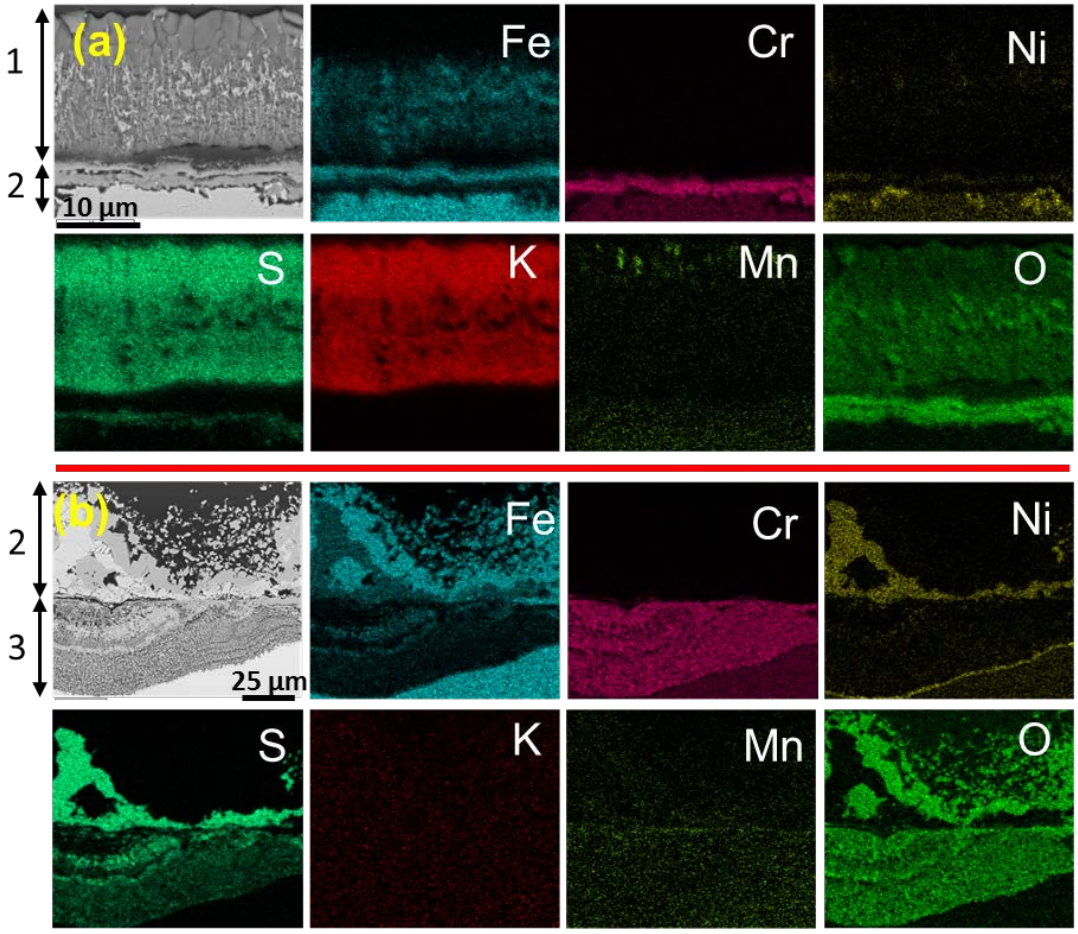

Figure 3. EDS maps showing elemental composition of the corrosion products resulting from exposure of deposit-coated samples to an oxidizing-sulphidizing gas mixture (experiment IIIa). Double-headed arrows 1–3 indicate the different layers of corrosion product. Note that the composition of layer 1 in (a) is similar in both Figures 2a and b, and hence not repeated in (b).

Figure 5 shows the corrosion product after partial removal of layer 1. From the overview in Figure 5a, the outward grown layers (i.e. layer 2) on regions with dome-like morphology (box b), layer 2 on regions with flat morphology (box c), as well as remnants of layer 1, can all be seen. Similar to the cross section of regions with a dome-like morphology (cf Figure 2b, c), the contrast in the magnified micrograph in Figure 5b also infers the presence of at least two phases, which is consistent with EDS analysis that the bright regions in this layer (area 2 in Figure 5b) are enriched in Fe, Ni, S and O, whereas the darker region consisting of finely dispersed particles (area 3 in Figure 5b) are enriched in Fe and O. Fe-rich larger faceted particles were also identified on some positions adjacent to the finely dispersed particles. Plan view investigations of regions with flat morphology show that a Fe-rich oxide layer exists below layer 1 on regions with a flat morphology, where no internal attack/pitting was observed (Figure 5c).

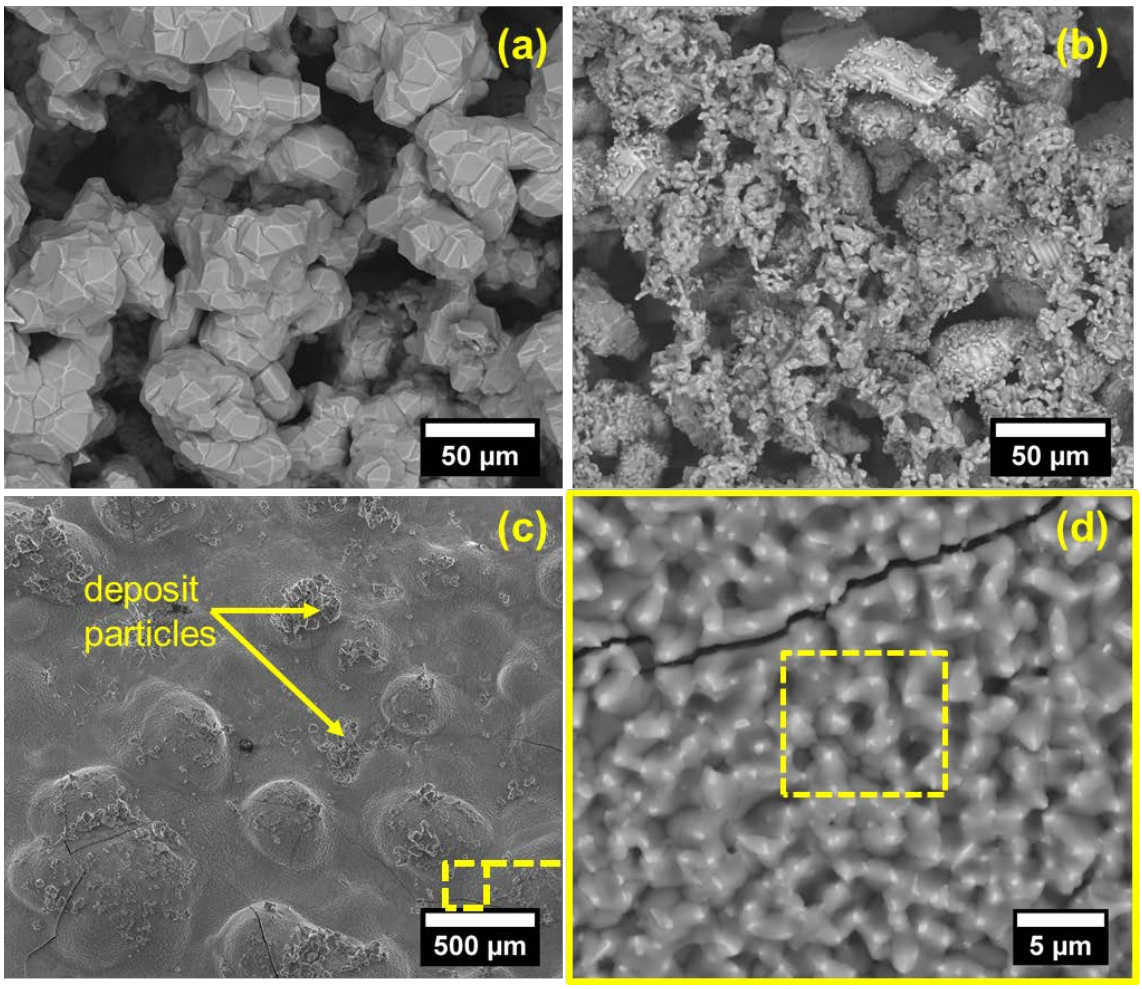

Figure 4. Plan view micrographs showing deposit particles at (a) the gas/deposit and (b) deposit/corrosion product interfaces after exposure to an oxidizing-sulphidizing gas mixture (experiment IIIa). (c) SE micrograph of layer 1 of corrosion product showing regions with both flat and dome-like (pitting) morphologies, below the initial deposit. (d) A magnified BSE micrograph of the flat regions contained in (c).

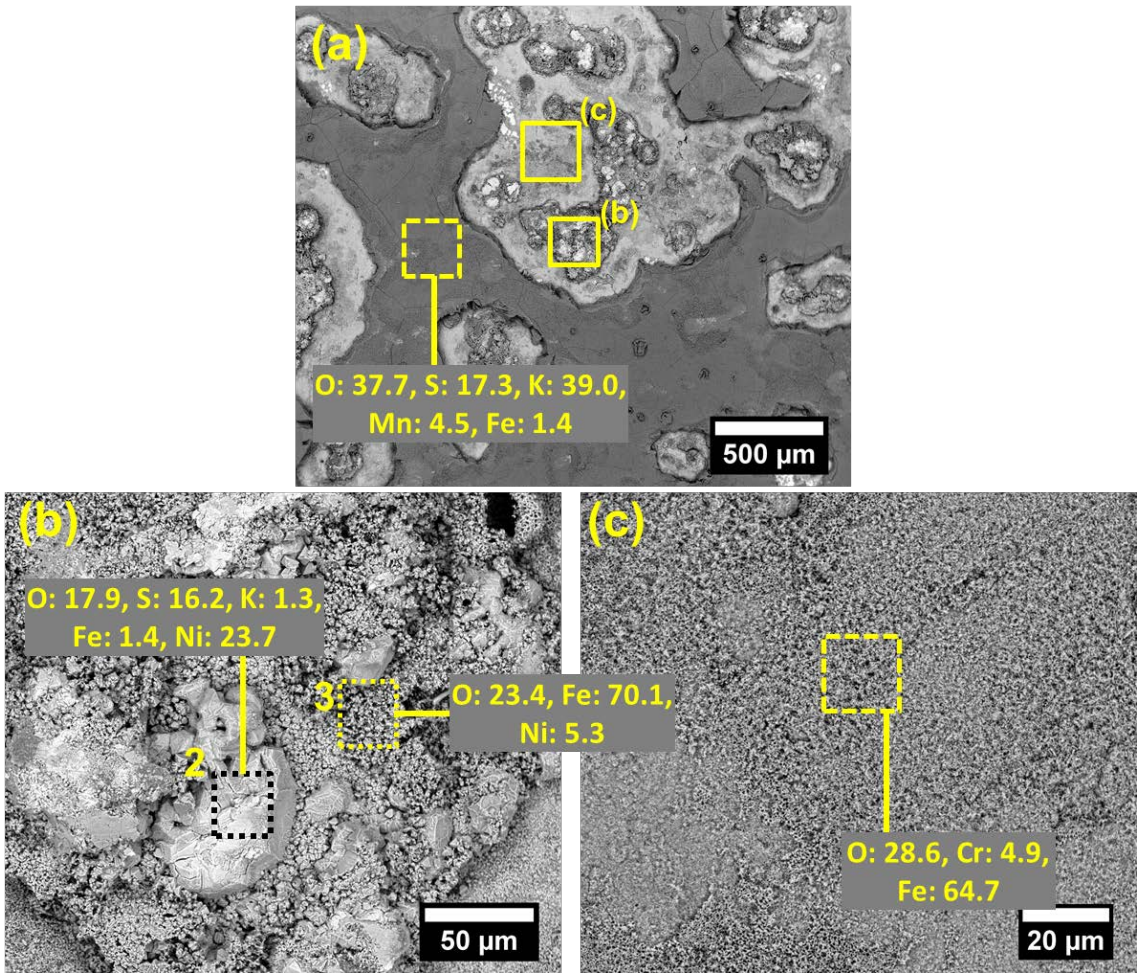

Figure 5. Plan view BSE micrograph after exposure of deposit-coated samples to an oxidizing-sulphidizing gas mixture (experiment IIIa) showing (a) an overview and (b,c) close-up microstructures of corrosion product below layer 1 (after partial removal of the layer shown in Figure 4c). Elemental compositions are given in wt%.

In Figure 6, the plan view of the corrosion products on the sample subsurface region is shown. Localized pits are observed in the micrograph corresponding to the internally attacked zones (layer 3) (cf. Figure 2). From the EDS maps, it is observed that these zones are depleted in Fe. In agreement with characterization on the cross section (Figure 3b), Cr, S, O are also present in the pits, and Ni is depleted within the pits but slightly enriched in the alloy adjacent to the pits. No additional feature was observed with further removal of the corrosion product, except for the reduction in size of the localized pits as the bulk of the alloy was approached.

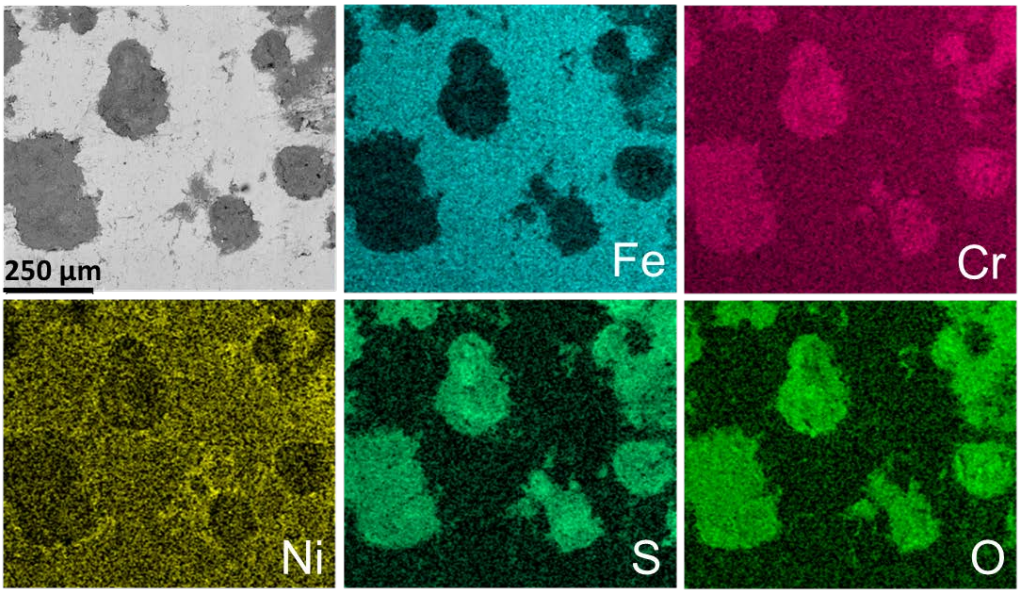

Figure 6. Plan view and EDS maps of the internally attacked region (layer 3) after exposure of deposit-coated samples to an oxidizing-sulphidizing gas mixture (experiment IIIa).

Phase identification through GI – XRD measurements (Figure 7), showed that the predominant crystalline corrosion product in layer 1 is K_2SO_4 [according to Joint Committee on Powder Diffraction Standards (JCPDS) card 05-613]. In addition, KCl was also identified in layer 1 due to incomplete removal of KCl deposit particles (cf. Figure 4c). On the external corrosion product layer beneath layer 1 (i.e. layers 2), the identified major crystalline phases were Fe_2O_3 (JCPDS card 33-664) and Fe_3O_4 (JCPDS card 73-698). Peaks from K_2SO_4 and KCl are still observed in the diffractogram recorded on the outward grown corrosion products, probably because of the incomplete removal of layer 1 (cf. Figure 5a). The diffractogram recorded on the sample subsurface (layer 3) is seen to contain peaks from Cr_2O_3 (JCPDS card 38-1479). Sulphides of Ni or Cr as suggested by EDS results in Figures 5 and 6 were not identified with XRD. Because the internally attacked regions are localized and thus the alloy bulk also diffracts, peaks from the austenite phase (alloy bulk) are also present in the diffractogram recorded on layer 3. The additional peak evolving near the austenite-111 peak at about $68^o2\theta$ (indicated by the arrow) originates from the stress-induced austenite transformation to martensite during the mechanical removal process. It is pertinent to note that the possibility of clarifying if oxides of the alloying elements are in solid solution in the identified phases cannot be determined based on the presented XRD results, because of the simultaneous influence of both chemical variations and internal stresses in the corrosion products on the measured peak positions compared to the theoretical diffraction angles of the various phases.

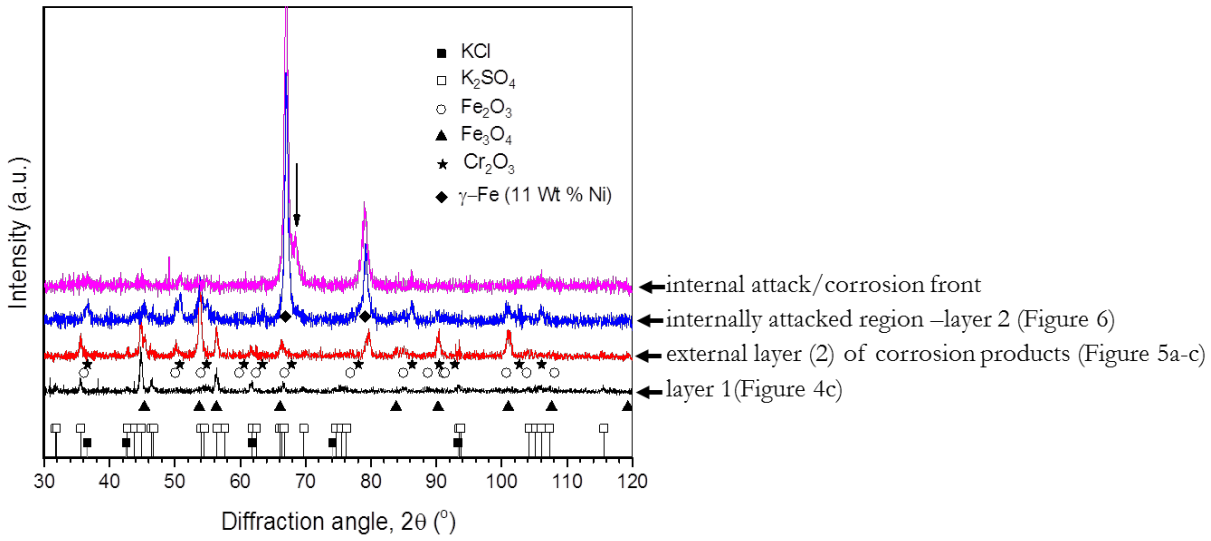

Figure 7. XRD diffractograms showing the crystalline phases present in different layers of the resulting corrosion product after exposure of deposit-coated samples to an oxidizing-sulphidizing gas mixture (experiment IIIa).

3.2 Deposit-free samples exposed to an oxidizing-sulphidizing gas (Experiment IIIb)

Figure 8 presents the cross-section and plan-view of the corrosion products after exposure of deposit-free samples to an oxidizing-sulphidizing gas. Compared to the corrosion product on deposit-coated samples, a relatively thin layer of corrosion product formed on deposit-free samples. Elemental maps (Figure 8a) of the O-rich corrosion product show that it is Fe-rich in the upper parts and Cr-rich in the lower parts. In addition, distinct S-containing regions are observed at the lower part of the corrosion product and, together with Ni, at points where the attack has occurred.

The plan view micrograph in Figure 8b show that the corrosion attack was somewhat minimized along the grain boundaries relative to the interior of the grains. By EDS mapping, it was observed that the corrosion products near the grain boundaries are Cr and Ni rich, whereas Fe-rich corrosion products are formed over the interior of the grains.

Fe_2O_3 (JCPDS card 33-664) and $FeCr_2O_4$ (JCPDS card 34-140) were the only crystalline corrosion products identified from GI – XRD measurements (Figure 9). As a result of the thin nature of corrosion products, peaks from the austenite phase (alloy bulk) were also recorded.

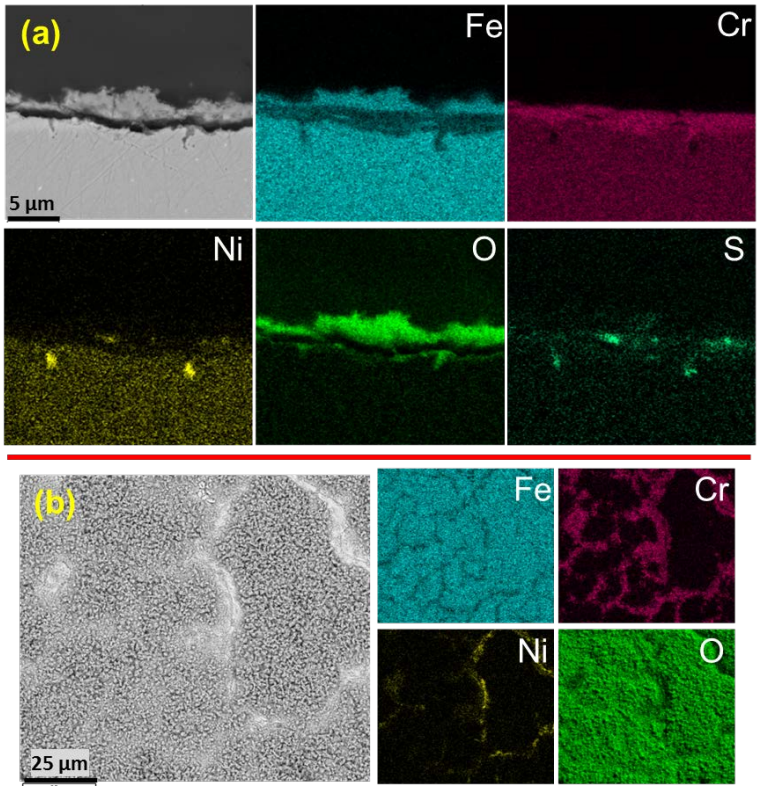

Figure 8. (a) Cross-section and corresponding EDS elemental maps, and (b) plan-view of the corrosion products resulting from exposure of deposit-free samples to an oxidizing-sulphidizing gas mixture (experiment IIIb).

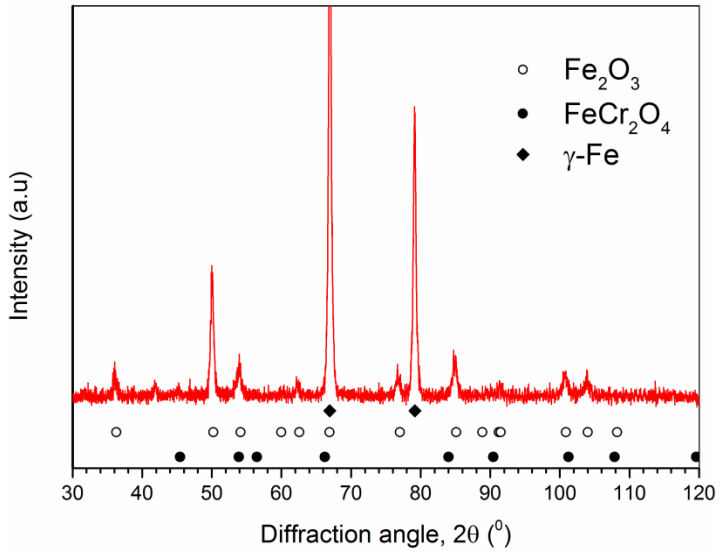

Figure 9. XRD diffractogram of a deposit-free sample exposed to an oxidizing-sulphidizing gas mixture (experiment IIIb).

3.3 KCl coated samples exposed to an oxidizing-sulphidizing-chlorinating gas (Experiment IVa)

The detailed results from cross-section and plan view characterization of corrosion products from this exposure have been previously reported by the present authors [30], where the effect of the water content in the corrosive gas mixture was addressed. In the present paper, a summary of results is presented to aid comparison with both experimental conditions IIIa in the present work, i.e. without HCl in the gas mixture, and experimental condition IIa in part I of this work [25], without SO_2 present in the gas mixture.

In general, three layers of corrosion products were observed below the initial deposit after exposure of deposit-coated samples to a gas mixture mimicking straw-firing, i.e. the oxidizing-sulphidizing-chlorinating gas mixture (Figure 10).

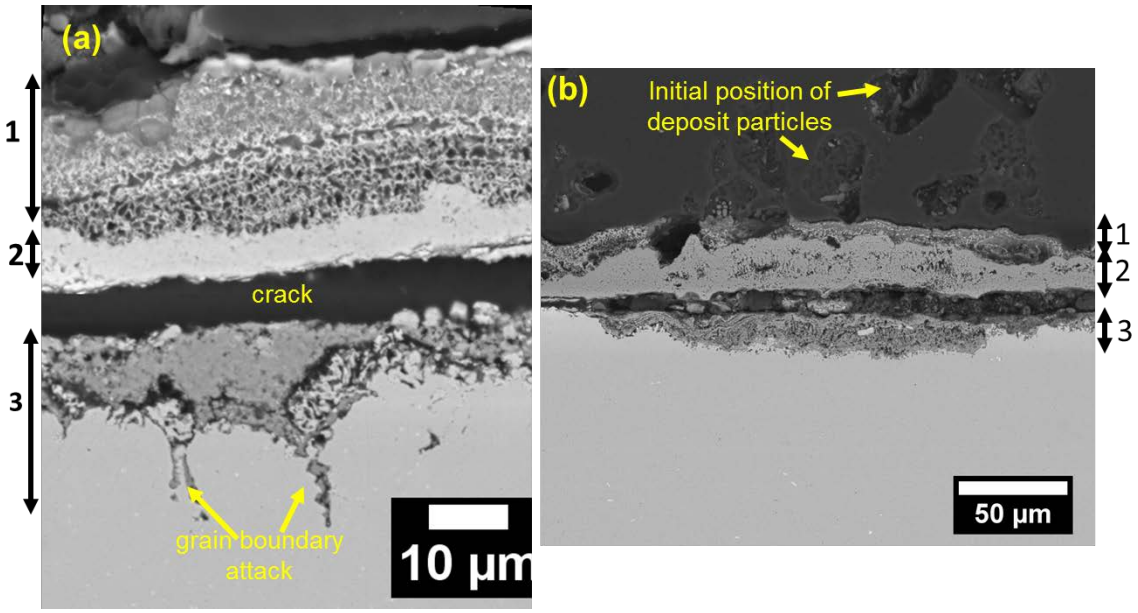

Figure 10. Resulting microstructures of the corrosion product after exposure of deposit-coated samples to the straw-firing gas mixture (experiment IVa). Inserted double-headed arrows indicate the different layers of corrosion product.

The different corrosion product layers are indicated by double-headed arrows in the micrographs shown in Figure 10a and b. Elemental mapping on the cross section (Figure 11a) show that K, S, Fe and O make up the elemental composition of layer 1. Additionally, Cl and K, and Mn and O were identified on some locations in the upper part of layer 1. The elemental composition of layer 2 revealed Fe, Cr and O. As is typical for deposit-induced corrosion, the morphology of the layer 3 was heterogeneous where grain boundary attack, selective attack resulting in porous regions and shallow S-containing pits were typical features observed. EDS mapping (Figure 11b) shows that layer 3 consists of Cr, Ni, S, and O. However,

Ni appears to be enriched in the regions with a porous morphology. Cl was also identified on some locations of layer 3 [30].

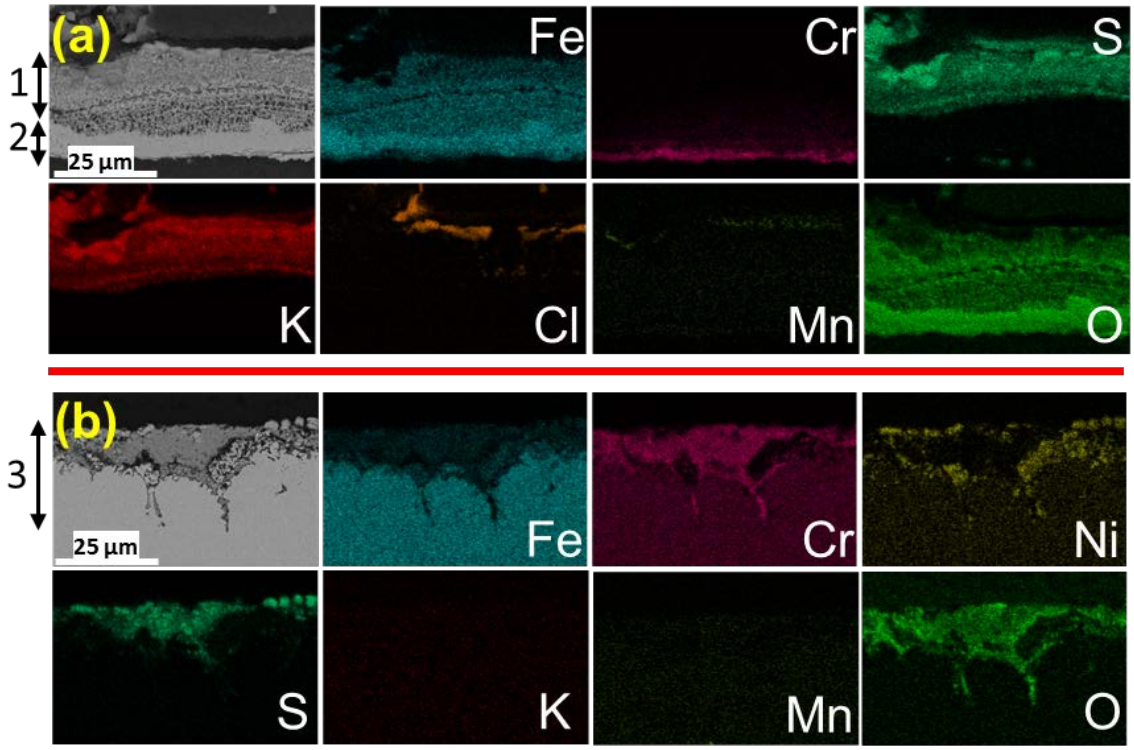

Figure 11. EDS maps showing the elemental composition of corrosion products resulting from the exposure of deposit-coated samples to a gas mixture mimicking straw-firing conditions (experiment IVa). Double-headed arrows 1–3 indicate the different layers of corrosion product.

Plan-view investigations showed K, S and O particles around original deposit particles due to partial sulphation of the KCl deposit both at the gas/deposit and deposit/corrosion product interfaces (Figures 12a and b, respectively). Similar to observations on the deposits exposed to an oxidizing-sulphidizing gas (cf. Figures 4a, b), accumulation of the K, S and O containing features occurred to a lesser extent at the deposit/corrosion product interface compared with the gas/deposit interface. Additionally, plan view investigations revealed that layer 1 was also composed of partially sulphated deposit particles on a K_2SO_4 –Fe_2O_3 –KCl layer (Figure 12c).

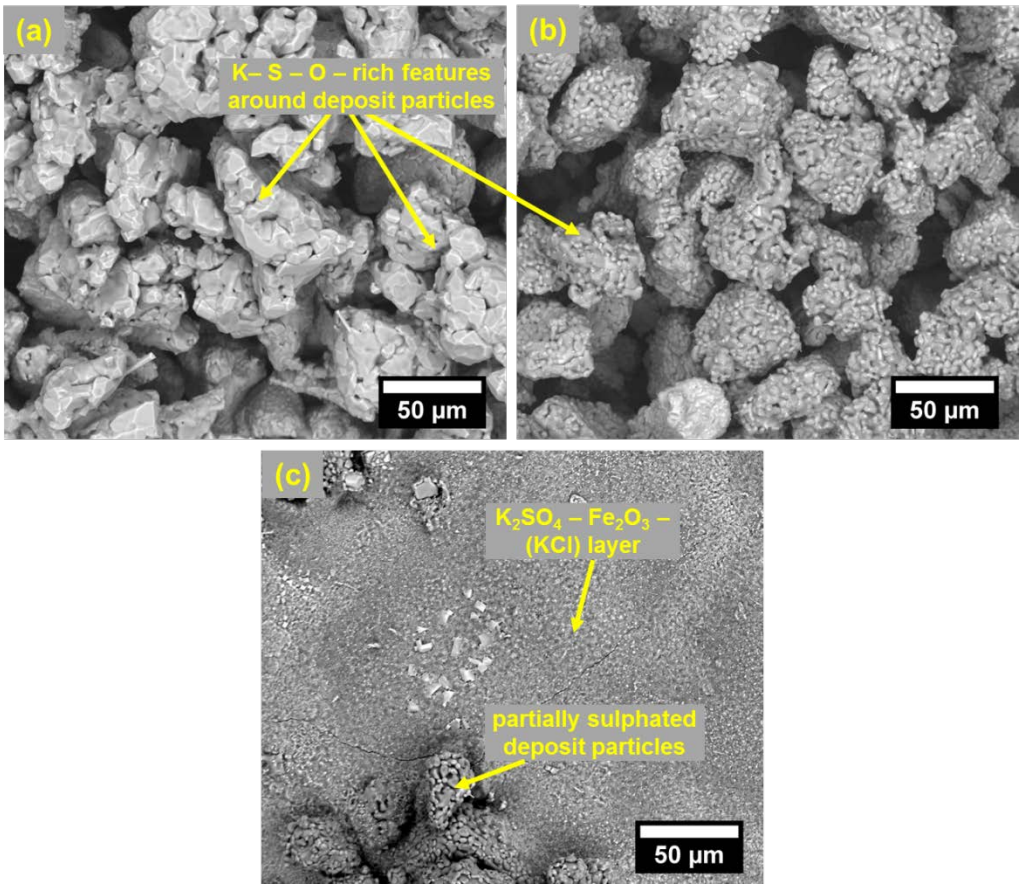

Figure 12. Plan-view microstructure of the deposit particles as observed from (a) the gas/deposit and (b) deposit/corrosion product interfaces. (c) Layer 1 of the corrosion product resulting from the exposure of deposit-coated samples to a gas mixture mimicking straw-firing conditions (experiment IVa).

3.4 Deposit-free samples exposed to an oxidizing-sulphidizing-chlorinating gas (Experiment IVb)

The plan-view micrograph in Figure 13 shows the corrosion products on a deposit-free sample after exposure to a gas mixture mimicking straw-firing. The contrast in the BSE micrograph suggests that a thicker layer of corrosion products formed mainly on the grain interiors (appearing darker) compared with regions around the grain boundaries, which appears brighter because of a higher fraction of backscattered electrons from the underlying bulk alloy. Similar to the composition of the corrosion products formed on deposit-free samples exposed to an oxidizing-sulphidizing gas (cf. Figure 8b), the corrosion product formed above the grain interiors was also Fe-rich compared with regions around the grain boundaries (Figure 13).

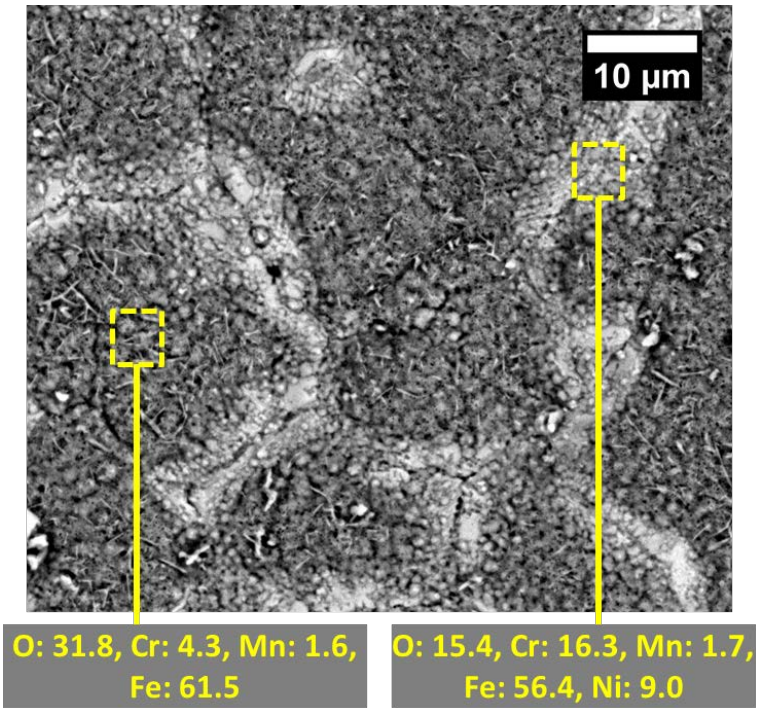

Figure 13. Plan-view microstructure and chemical composition (in wt %) of the corrosion product observed after the exposure of deposit-free samples to a gas mixture mimicking straw-firing conditions (experiment IVb).

3.5 Thickness of corrosion products

Statistical variation in thickness of the first layer of corrosion products (layer 1) resulting from exposure of deposit-coated samples to the different atmospheres are compared in Figure 14. Comparisons of the mean and maximum values show that exposure of deposit-coated samples to an oxidizing-sulphidizing atmosphere results in a thicker sulphate (K_2SO_4) containing layer – layer 1. In Figure 14, the depths of internal attack suffered by deposit-coated samples exposed to the different atmospheres are also compared, to obtain a measure of corrosion rate in the different atmospheres. Comparison of the internally attacked layer considered the depth of the broad pits (layer 3 in Figure 2) after exposures under oxidizing-sulphidizing atmospheres, and the thickness of layer 3 (Figure 10) from exposures to straw-firing conditions. It is observed that both the mean and maximum depth of the pits resulting from exposure to an oxidizing-sulphidizing gas surpasses the mean and maximum depth of internal or grain boundary attack resulting from exposure to the gas mixture mimicking straw-firing.

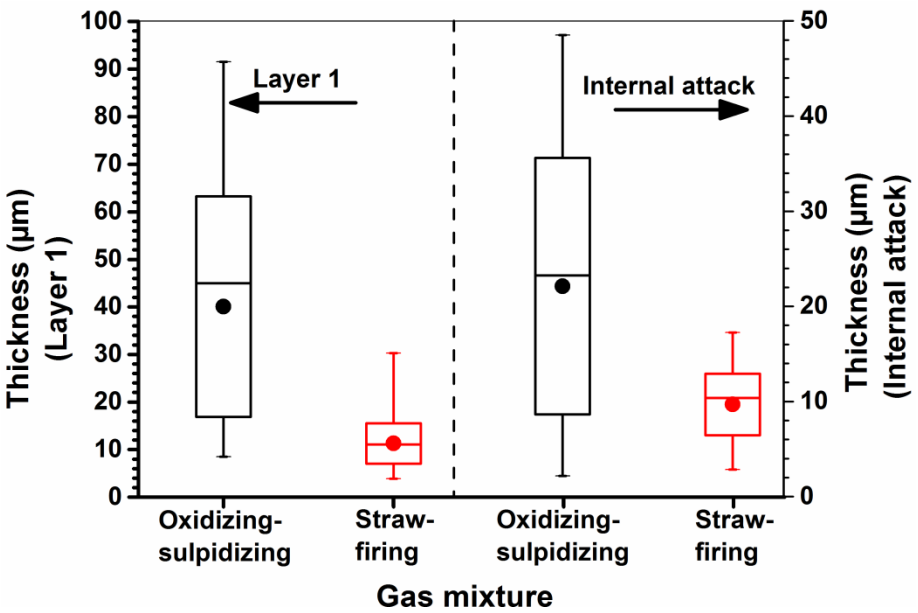

Figure 14. Thicknesses of layer 1 of corrosion product, and the internal attack after exposure of deposit-coated samples to the different gas mixtures. The maximum and minimum values are represented by marks above and below each box, whereas location of 50 % of the distribution is shown by the horizontal bar in each box. Round dots in each box represent the mean value, and the standard deviation from the mean is represented by the horizontal edges of the box. At least 20 positions on the exposed samples were measured to obtain the distribution. Note the difference in the vertical scales.

4 Discussion

From characterization of the samples exposed to the different atmospheres, it is revealed that more corrosion attack occurred on deposit-coated samples compared with deposit-free samples exposed to identical conditions. A summary of the corrosion products identified on deposit-coated samples is presented in Table 2 to aid comparison. A noteworthy observation is that partial sulphation of the deposit particles occurred after exposure to both an oxidizing-sulphidizing gas (Figure 4a, b) and an oxidizing-sulphidizing-chlorinating gas (mimicking straw-firing) (Figure 12a, b). As a result, metal oxides of Fe and Mn, in mixture with K_2SO_4 were always present in layer 1 of the corrosion product (i.e. below the deposit) with a morphology that indicated formation of a melt phase during the exposure. KCl was present in some cases in layer 1. The elemental composition and morphology of layer 3 of corrosion products after the exposures remarkably depended on the absence/presence of additional HCl in the gas mixture. In the following discussion, the interactions between the alloying elements, deposit (KCl) particles, and the gaseous atmosphere are addressed in terms of their impact on corrosion under conditions relevant to biomass-firing.

Table 2. Summary of corrosion products on deposit-coated samples resulting from exposure to the different gas mixtures.

Experiment	Deposit appearance	Corrosion product morphology, phase and chemical composition
IIIa (oxidizing-sulphidizing gas mixture)	Partly sulphated at both gas/deposit and deposit/corrosion product interfaces	**Flat morphology**: layer 1: Flat and partly molten, K_2SO_4 and Fe_2O_3 Layer 2: Fe – Cr – rich oxide. Ni and S enrichment in deeper regions **Flat morphology**: layer 1: Flat and partly molten, K_2SO_4 and Fe_2O_3 Layers 2: Fe – O and Ni – S rich regions, Fe_2O_3 and Fe_3O_4 Layer 3: Broad internal Cr – O – S-rich pits, Cr_2O_3, Ni enrichment at interface between pits and bulk alloy
IIIb (oxidizing-sulphidizing gas-mixture)		Discontinuous Fe-Cr-rich oxide, Fe_2O_3. Local S enrichment
IVa (oxidizing-sulphidizing-chlorinating gas mixture)	Partly sulphated at both gas/deposit and deposit/corrosion product interfaces	Layer 1: Partly molten, K_2SO_4 and Fe_2O_3, and KCl Layer 2: Fe – Cr – rich oxide, Fe_2O_3 Layer 3: Cr – Ni – S – O – rich, grain boundary attack, chlorine rich features
IVb (oxidizing-sulphidizing-chlorinating gas-mixture)		Discontinuous Fe-Cr-rich oxide, Fe_2O_3 [30]

4.1 SO_2 effects in the presence of a KCl deposit

In part-I of this work, the effect of a KCl deposit on corrosion of samples exposed under oxidizing conditions was discussed [25]. Potassium from the deposits was suggested to disrupt the initial protective layer (Cr_2O_3) causing the formation of a non-protective Fe-rich layer instead [10]. Subsequently, due to the ability of chlorine species (both from such reaction and the HCl in the gas mixture) to initiate chlorination of alloying elements, selective attack of Fe, Mn and Cr was observed. The reaction between KCl with Cr_2O_3 may have occurred in the present study. As reported in [7,16], formed K_2CrO_4 will be quickly sulphated to K_2SO_4 due to the presence of SO_2 in the gas mixtures.

A positive effect of SO_2 has been reported when SO_2 sulphates KCl aerosol particles in the vapour phase, before they condense on vulnerable metallic surfaces (i.e. 'in-flight' sulphation) [31,32].

However, heterogeneous ('in-deposit') sulphation [33] is considered in the following discussion because this corresponds to the experimental conditions in the present study. This reaction is responsible for the accumulation of K, S and O-rich (K_2SO_4) features around KCl particles and is in agreement with results from full-scale studies [12]. The mechanism behind this is properly discussed in literature [33–35].

According to the Deacon process [36], the sulphation of KCl particles under the current experimental conditions will result in generation of p_{Cl_2} which is six orders of magnitude higher than that resulting from K_2CrO_4 formation [29,28]. A pertinent question would be how this 'in-deposit' sulphation reaction will influence corrosion of the alloy with respect to the formed sulphate and released HCl.

For the deposit-coated samples exposed to gas mixtures containing SO_2, the simultaneous presence of both K_2SO_4 and M_xO_y ($M = \{Fe, Mn\}$) is observed in layer 1 below the deposits. This therefore suggests that metal (Fe and Mn) chlorides formed due to chlorination (reaction 1) and were converted to their oxides within the sulphate.

$$M(s) + xCl \rightleftharpoons MCl_x(s) \qquad (1)$$

Plan view investigations (Figures 4d and 12c) show that layer 1 has partly been molten although the exposure temperature in this work (560 °C) was considerably lower than the melting temperature of K_2SO_4 (1069 °C), KCl (772 °C) and the KCl-K_2SO_4 eutectic temperature (690 °C) [37]. Interestingly, the KCl-K_2SO_4-Fe_2O_3 system has been reported to show a solidus at 577 °C [38]. It is therefore possible that the metal chlorides generated from reaction 1 during the initial stages of corrosion lowered the melting temperature of the KCl-$MeCl_x$-K_2SO_4 system below 560 °C. Metal chlorides (especially $FeCl_2$) are known [7,38,39], and was also observed in part 1 of this study [25] to be able to induce low temperature melt formation. In accordance with increased generation of HCl reported in reference [33], such solid-liquid transformation enhances the rate of the sulphation reaction because KCl sulphates faster in the molten phase. In addition, a better coverage of the sample is provided by the Cl-containing melt, hence, permitting greater dissolution of alloying element by chlorination.

Molten sulphate deposits have the potential of initiating hot corrosion attack at temperatures above 600°C [40]. The morphology of corrosion products formed on KCl deposit-coated samples exposed to oxidizing-sulphidizing gas mixture (Figures 2 and 5) suggests corrosion attack dominated by molten sulphates and in addition, it is similar to that observed for a Co-Cr alloy exposed at temperatures between 600 and 750 °C [41]. However, the absence of K in the large pits (Figure 3b) implies that the mechanism of corrosion attack of the present samples is not solely related to the previously outlined type (II) hot corrosion caused by a related sulphate (Na_2SO_4) [41,42]. Although dissolution of alloying elements in the sulphate melt has been reported [43] as the major mechanism of attack responsible for the formation of the observed large pits (Figure 2b), a synergistic action between Cl and S may be responsible for the increased corrosion attack after exposure to an oxidizing-sulphidizing gas. Thus, it is suggested that in the Cl-containing melt, dissolution occurred by chlorination (reaction 1) of alloying elements. This is supported by the presence of Ni-rich porous

layers on some positions adjacent to the corrosion front (Figure S1, supporting information) because, compared to Fe, Cr and Mn, Ni has a lower driving force for chlorination [36,44,45]. A similar synergistic effect (between Cl and S) has also been observed for corrosion attack under a syngas atmosphere [46] and with sulphate deposits [47] due to the additional influence of chlorides. In addition to the proposed role of both KCl and metal chlorides to assist in low temperature formation of a sulphate containing melt, these Cl-bearing species are also proposed to assist in transportation of alloying elements away from the corrosion front (in the pits) leading to their redistribution above the pits. Some considerations on the mechanisms leading to this complex corrosion attack are further discussed as follows.

Upon chlorination of alloying elements in the melt, volatile metal chlorides with varying stabilities will result [36,44,45]. Specifically, Fe and Ni-chlorides, according to thermodynamic calculations [29,28] will need to encounter sufficiently higher p_{O_2} ($> 10^{-27}$ and 10^{-21} atm, respectively), to be converted to the corresponding metal oxides (reaction 2), compared to Cr which will require $p_{O_2} > 10^{-38}$ atm. The requirement of high p_{O_2} for $NiCl_2$ transformation to the oxide is supported by experimental results in reference [21] as well as its observation on samples after in situ corrosion tests in power plants [48].

$$yMCl_x(g) + \frac{z}{2}O_2(g) \rightleftharpoons M_yO_z(s) + yCl_x(g) \qquad (2)$$

In agreement with thermodynamic calculations with respect to p_{O_2}, only Ni- and Fe-containing corrosion products were observed above the pits (Figure 3b). The resulting metal chlorides of these elements were partitioned into Fe-oxide and Ni-sulphide, which is justified on the basis of the corresponding reactions between $FeCl_2$ and $NiCl_2$ resulting from chlorination within the pits, and S-containing species at positions above the pits. The thermodynamic favourability of reaction 3 ($\Delta G° = -85.93$ kJ/mol (NiS) at 560 °C [28,29]) supports favourable partitioning of Ni into the sulphide phase and Fe as the oxide as observed in Figure 3b. (FeS and NiS have been chosen for simplicity).

$$FeS(s) + NiO\ (s) + 0.16O_2(g) \rightleftharpoons 0.33Fe_3O_4(s) + NiS(s) \qquad (3)$$

As a result of the porous morphology of the corrosion product in the pits (Figure 2b), transport of SO_2 into the pits is also feasible, and in addition to low p_{O_2} present in these regions, sulphidation of Fe can occur, as confirmed experimentally in the EDS maps in Figure 3b. Moreover, reaction of the resulting Fe-sulphides with Cl species would also result in formation of the volatile Fe-chlorides which will be transported away from the pits in accordance with the active-sulphidation mechanism proposed in reference [49]. Interestingly, the very low p_{O_2} in the pits is also observed to be sufficient for conversion of any $CrCl_2$ to the oxide.

The morphology of the corrosion products resulting from experiments IIIa and IVa (cf. Figures 2 and 10) as well as the degree of corrosion attack (cf. Figure 14) suggests that with SO_2 in the gas mixture, the type of corrosion attack depends on whether HCl is also present in the gas mixture. The presence of HCl in the oxidizing-sulphidizing-chlorinating gas mixture, (simulating straw-firing) is observed to reduce the thickness of the $K_2SO_4 - M_xO_y$ layer (Figure 14), which is probably caused by

decreased sulphation of KCl to K_2SO_4. Comparison of corrosion product morphologies (cf. Figures 2 and 10) reveals that the suspected Cl-assisted hot-corrosion attack was greatly reduced in the oxidizing-sulphidizing-chlorinating environment possibly because the sulphate layer was not able to provide a slightly reducing microclimate to facilitate such corrosion attack. However, selective chlorination of Fe, Mn and Cr (reaction 1) occurred and accounts for the formation of porous Ni-rich islands in layer 3 of the corrosion product (Figures 10a and 11b). Furthermore, the tendency of Cl to perpetuate corrosion attack along grain boundaries due to easier diffusion along these paths (as was observed in part I of this study, under oxidizing and oxidizing-chlorinating conditions [25]), is also manifested in the corrosion products. Nonetheless, formation of Cr-rich shallow pits (Figure 10b) similar to those observed from the oxidizing-sulphidizing gas mixture (cf. Figure 2b), in addition to accumulation of S in the lower layers of corrosion product (Figure 11b) also infers that in addition to chlorination, sulphidation has an essential influence on the observed corrosion attack.

From comparison of the results in part I of this study [25], and the present results, it is observed that KCl interaction with metal chlorides always results in melt formation, which increases corrosion attack. However, contrary to the oxidizing and oxidizing-chlorinating conditions, the sulphate layers resulting from sulphation in SO_2 containing gases provides microclimates which facilitate severe pitting attack. To improve the understanding of SO_2 effects on high temperature corrosion involving KCl deposits, as well as the responsible mechanisms, further experiments should be conducted by varying parameters such as SO_2 concentration within ranges relevant to biomass firing, deposit thickness, oxidizing potential of the gas, as well as the use of K_2SO_4 as the initial deposit. Time resolved studies are also necessary to observe corrosion in the initial stages.

4.2 SO_2 effects under deposit-free conditions

The morphology of corrosion products resulting from exposure of deposit-free samples suggests a lesser degree of corrosion attack relative to that on the deposit-coated samples. Interestingly, the corrosion product morphology and composition was similar for deposit-free samples exposed to both oxidizing-sulphidizing gas (cf. Figure 8b) and the gaseous mixture mimicking straw-firing conditions (cf. Figure 13). Comparison of the experimental results after exposures to oxidizing and oxidizing-chlorinating atmospheres in the absence of a KCl deposit (see part-I of this study [25]) with the present results from oxidizing-sulphidizing and straw-firing atmospheres, reveals that the formation of a double layered corrosion product was strongly inhibited after exposures to gas mixtures containing SO_2. This effect could be attributed to strong adsorption of SO_2 on active sites of the sample surface, consequently hampering formation of oxygen containing ions [18]. In line with this, the kinetics of oxidation will be reduced as a result of the limited adsorption of oxygen bearing species (which generate oxygen containing anions). In addition to the active site blocking effect, adsorbed sulphate species may influence the transport of ions through the oxide grain boundaries. Surface sulphates has been suggested to slow down oxygen ion transport in the grain boundary of hematite, thereby causing an inhibitive effect on the oxidation of Fe [18].

On the other hand, previous investigation on the oxidation of FeCr alloys has suggested that the development of a double layered corrosion product facilitated by H ingress into the alloy [50], is

greatly reduced by the presence of impurity S in the alloy [51]. The high affinity of Cr for S promoted its enrichment around segregated S regions, and was mooted to enhance formation of the protective Cr_2O_3 [51]. Interestingly, EDS maps in Figure 8 reveal that after exposure of deposit-free samples to an oxidizing-sulphidizing gas (experiment IIIb), S accumulated in the lower parts of the corrosion products and along the attacked grain boundaries. It is possible that this facilitated formation of Cr-rich oxides which slowed down growth of the double layered oxide observed in SO_2 free exposures [25].

In all the gas mixtures utilized for exposures in the present study (Table 1), the ratio of $\mathbf{p_{H_2O}}$ to $\mathbf{p_{O_2}}$ is greater than 1, hence an additional effect of this high $\mathbf{p_{H_2O}}$ on corrosion is possible. High $\mathbf{p_{H_2O}}$ in the O_2 containing gas mixture is known to cause volatilization of Cr oxide in the form of $CrO_2(OH)_2$ species even at temperatures below 1000 °C, above which oxide volatilization has been suggested to account for accelerated corrosion [10,52]. Above 500 °C, it has been observed for austenitic stainless steels, that Cr-depleted oxides are consequently formed due to insufficient supply of Cr from the bulk to maintain formation of a Cr-rich oxide [10][53]. This effect is also reflected in results observed on deposit-free samples after exposure to oxidizing-sulphidizing and oxidizing-sulphidizing-chlorinating (straw-firing) gas mixtures. Mainly Fe-rich oxides were observed by plan-view investigations (cf. Figures 8b and 13). However, the regions surrounding the grain boundaries show the presence of a thinner Cr-rich oxide which was facilitated by faster transport of Cr through the grain boundaries. In addition to the possible effect of Cr-oxide volatilization, the formation of Fe-rich oxides may have been induced by the ability of OH^- resulting from dissociation of H_2O, to promote internal oxidation of Cr, thereby resulting in the outward formation of Fe-rich oxides [54].

5 Summary and conclusions

The effects of flue gas composition on high temperature corrosion of a superheater material (TP 347H FG) have been studied, with emphasis on the role of 60 ppmv SO_2 in the gas. The following conclusions can be made based on the obtained results.

- SO_2 in the gas phase is able to reduce corrosion attack only in the absence of a KCl deposit.

- Deposit-coated samples suffer more corrosion attack compared to their deposit-free counterparts after similar exposure to SO_2 containing gas mixtures.

- SO_2 incorporation into the gas phase causes sulphation of the original KCl deposit particles. A layer comprising mainly of K_2SO_4 and Fe_2O_3 forms below the initial deposit. The Fe_2O_3 in this layer results from conversion of metal chlorides to oxides.

- In the presence of KCl, a chloride-sulphate melt induced by metal chlorides forms, and provokes a Cl-assisted pitting attack. Alloying elements are chlorinated and transported as metal chlorides away from the pits. This type of corrosion attack is severe under an oxidizing-sulphidizing gas atmosphere.

- Additional presence of HCl in the gas mixture (oxidizing-sulphidizing-chlorinating gas mixture) decelerates the pitting attack but initiates grain boundary attack.

- The severe degradation suffered by deposit-coated samples after exposure to an oxidizing-sulphidizing gas mixture hint at possible corrosion problems if 'in-deposit' sulphation of alkali chlorides occurs under low p_{O_2} conditions.

Acknowledgements

This work is part of the Danish Strategic Research Centre, Power Generation from Renewable Energy (GREEN). The authors acknowledge funding from the Danish council for Strategic Research.

References

[1] M. Montgomery, A. Karlsson, In-situ corrosion investigation at Masnedø CHP plant - a straw-fired power plant, Mater. Corros. 50 (1999) 579–584.

[2] F.J. Frandsen, Ash Formation, Deposition and Corrosion when Utilizing Straw for Heat and Power Production, Dr. Techn. Thesis, Department of Chemical and Biochemical Engineering, Technical Univeristy of Denmark. ISBN: 9788792481405, Kongens Lyngby, 2011.

[3] M. Montgomery, A. Karlsson, O.H. Larsen, Field test corrosion experiments in Denmark with biomass fuels. Part 1: Straw-firing, Mater. Corros. 53 (2002) 121–131.

[4] S. V. Vassilev, D. Baxter, L.K. Andersen, C.G. Vassileva, T.J. Morgan, An overview of the organic and inorganic phase composition of biomass, Fuel. 94 (2012) 1–33.

[5] C. Pettersson, J. Pettersson, H. Asteman, J.-E. Svensson, L.-G. Johansson, KCl-induced high temperature corrosion of the austenitic Fe–Cr–Ni alloys 304L and Sanicro 28 at 600°C, Corros. Sci. 48 (2006) 1368–1378.

[6] R.A. Antunes, M.C.L. de Oliveira, Corrosion in biomass combustion: A materials selection analysis and its interaction with corrosion mechanisms and mitigation strategies, Corros. Sci. 76 (2013) 6–26.

[7] S.C. Okoro, M. Montgomery, F.J. Frandsen, K. Pantleon, High Temperature Corrosion under Laboratory Conditions Simulating Biomass-Firing: A Comprehensive Characterization of Corrosion Products, Energy & Fuels. 28 (2014) 6447–6458.

[8] J. Lehmusto, D. Lindberg, P. Yrjas, B.-J. Skrifvars, M. Hupa, Thermogravimetric studies of high temperature reactions between potassium salts and chromium, Corros. Sci. 59 (2012) 55–62.

[9] W.B.A. Sharp, Superheater Corrosion in Biomass Boilers : Today's Science and Technology, 2011.

[10] J. Pettersson, J.-E. Svensson, L.-G. Johansson, KCl-Induced Corrosion of a 304-type Austenitic Stainless Steel in O2 and in O2 + H2O Environment: The Influence of Temperature, Oxid. Met. 72 (2009) 159–177.

[11] P.A. Jensen, F.J. Frandsen, J. Hansen, K. Dam-Johansen, N. Henriksen, S. Hörlyck, SEM Investigation of Superheater Deposits from Biomass-Fired Boilers, Energy & Fuels. 18 (2004) 378–384.

[12] L.A. Hansen, H.P. Nielsen, F.J. Frandsen, K. Dam-Johansen, S. Hørlyck, A. Karlsson, Influence of deposit formation on corrosion at a straw-fired boiler, Fuel Process. Technol. 64 (2000) 189–209.

[13] J.N. Knudsen, P.A. Jensen, W. Lin, F.J. Frandsen, K. Dam-Johansen, Sulfur Transformations during Thermal Conversion of Herbaceous Biomass, Energy & Fuels. 18 (2004) 810–819.

[14] J.M. Johansen, J.G. Jakobsen, F.J. Frandsen, P. Glarborg, Release of K, Cl, and S during Pyrolysis and Combustion of High-Chlorine Biomass, Energy & Fuels. 25 (2011) 4961–4971.

[15] K.A. Christensen, M. Stenholm, H. Livbjerg, The formation of submicron aerosol particles, HCl and SO2 in straw-fired boilers, J. Aerosol Sci. 29 (1998) 421–444.

[16] S. Karlsson, T. Jonsson, J. Hall, J.-E. Svensson, J. Liske, Mitigation of Fireside Corrosion of Stainless Steel in Power Plants: A Laboratory Study of the Influences of SO2 and KCl on Initial Stages of Corrosion, Energy & Fuels. 28 (2014) 3102–3109.

[17] S. Karlsson, J. Pettersson, J.E. Svensson, L.G. Johansson, KCl-Induced High Temperature Corrosion of the Austenitic Stainless Steel 304L – The Influence of SO2, Mater. Sci. Forum. 696 (2011) 224–229.

[18] A. Järdnäs, J.-E. Svensson, L.-G. Johansson, The Inhibitive Effect of Traces of SO2 on the Oxidation of Iron, Oxid. Met. 60 (2003) 427–445.

[19] J. Pettersson, J.E. Svensson, L.G. Johansson, Alkali Induced Corrosion of 304-Type Austenitic Stainless Steel at 600°C; Comparison between KCl, K2CO3 and K2SO4, Mater. Sci. Forum. 595-598 (2008) 367–375.

[20] D.A. Vaughan, H.H. Krause, W.K. Boyd, Chloride corrosion and its Inhibition in refuse firing, in: R.W. Bryers (Ed.), Impurities Combust. Gases, MCGraw-Hill, 1978: pp. 473–493.

[21] M. Paneru, G. Stein-Brzozowska, J. Maier, G. Scheffknecht, Corrosion Mechanism of Alloy 310 Austenitic Steel beneath NaCl Deposit under Varying SO2 Concentrations in an Oxy-fuel Combustion Atmosphere, Energy & Fuels. 27 (2013) 5699–5705.

[22] H.P. Michelsen, F.J. Frandsen, K. Dam-Johansen, O.H. Larsen, Deposition and high temperature corrosion in a 10 MW straw fired boiler, Fuel Process. Technol. 54 (1998) 95–108.

[23] M. Montgomery, L. V Nielsen, M.B. Petersen, Utilization of on-line corrosion monitoring in the flue gas cleaning system, in: Proc. NACE Corros., 2015.

[24] J.N. Knudsen, O.H. Larsen, M. Montgomery, O. Biede, P.J. Jensen, Deposit formation and corrosion in straw-fired boilers - firing trials in AVV2 bioboiler (PSO-project FU 1202 Report), 2005.

[25] S.C. Okoro, S. Kiamehr, M. Montgomery, F.J. Frandsen, K. Pantleon, Effect of flue gas composition on deposit induced high temperature corrosion under laboratory conditions mimicking biomass firing. Part I: Exposures in oxidizing and chlorinating atmospheres, Mater. Corros. 68 (2017) 499–514.

[26] S. Kiamehr, K.V. Dahl, M. Montgomery, M.A.J. Somers, KCl-induced high temperature corrosion of selected commercial alloys. Part I: chromia-formers, Mater. Corros. 66 (2015) 1414–1429.

[27] H.P. Nielsen, F.J. Frandsen, K. Dam-Johansen, Lab-Scale Investigations of High-Temperature Corrosion Phenomena in Straw-Fired Boilers, Energy & Fuels. 13 (1999) 1114–1121.

[28] What's New in FactSage 7.0, (2015). http://www.crct.polymtl.ca/fact/facthelp/FS70New.htm (accessed June 2, 2016).

[29] C.W. Bale, E. Bélisle, P. Chartrand, S.A. Decterov, G. Eriksson, K. Hack, I.-H. Jung, Y.-B. Kang, J. Melançon, A.D. Pelton, C. Robelin, S. Petersen, FactSage thermochemical software and databases — recent developments, Calphad. 33 (2009) 295–311.

[30] S.C. Okoro, M. Montgomery, F.J. Frandsen, K. Pantleon, Effect of Water Vapor on High-Temperature Corrosion under Conditions Mimicking Biomass Firing, Energy & Fuels. 29 (2015) 5802–5815.

[31] M. Aho, P. Vainikka, R. Taipale, P. Yrjas, Effective new chemicals to prevent corrosion due to chlorine in power plant superheaters, Fuel. 87 (2008) 647–654.

[32] H. Wu, J.B. Jespersen, F.J. Frandsen, P. Glarborg, M. Aho, K. Paakkinen, R. Taipale, Modeling of ferric sulfate decomposition and sulfation of potassium chloride during grate-firing of biomass, AIChE J. 59 (2013) 4314–4324.

[33] L.W. Sengeløv, T.B. Hansen, C. Bartolome, H. Wu, K.H. Pedersen, F.J. Frandsen, A.D. Jensen, P. Glarborg, Sulfation of Condensed Potassium Chloride by SO 2, Energy & Fuels. 27 (2013) 3283–3289.

[34] L. Boonsongsup, K. Iisa, W.J. Frederick, Kinetics of the Sulfation of NaCl at Combustion Conditions, Ind. Eng. Chem. Res. 5885 (1997) 4212–4216.

[35] K. Iisa, Y. Lu, K. Salmenoja, Sulfation of Potassium Chloride at Combustion Conditions, Energy & Fuels. 13 (1999) 1184–1190.

[36] A. Zahs, M. Spiegel, H. Grabke, The influence of alloying elements on the chlorine-induced high temperature corrosion of Fe-Cr alloys in oxidizing atmospheres, Mater. Corros. 50 (1999) 561–578.

[37] FactSage, www.factsage.com, (2014). http://www.crct.polymtl.ca/factsage/fs_general.php (accessed December 10, 2014).

[38] H.P. Nielsen, Deposition and High-temperature Corrosion in Biomass-Fired Boilers, PhD Thesis, Technical University of Denmark, 1998.

[39] A. Karlsson, P.J. Møller, V. Johansen, Iron and steel corrosion in a system of 02,S02 and alkali chloride. The formation of low melting point salt mixtures, Corros. Sci. 30 (1990) 153–158.

[40] R.A. Rapp, Chemistry and electrochemistry of hot corrosion of metals, Mater. Sci. Eng. 87 (1987) 319–327.

[41] K.L. Luthra, Low Temperature Hot Corrosion of Cobalt-Base Alloys: PartI. Morphology of the Reaction Product, Metall. Trans. A. 13 (1982) 1843–1852.

[42] K.L. Luthra, D.A. Shores, Mechanism of Na2SO4 Induced Corrosion at 600°–900°C, J. Electrochem. Soc. 127 (1980) 2202.

[43] K.L. Luthra, Low Temperature Hot Corrosion of Cobalt-Base Alloys: Part II. Reaction Mechanism, Metall. Trans. A. 13 (1982) 1853–1864.

[44] R. Bender, M. Schütze, The role of alloying elements in commercial alloys for corrosion resistance in oxidizing-chloridizing atmospheres part I: Literature evaluation and thermodynamic calculations on phase stabilities, Mater. Corros. 54 (2003) 567–586.

[45] M.C. Galetz, B. Rammer, M. Schütze, Refractory metals and nickel in high temperature chlorine-containing environments - thermodynamic prediction of volatile corrosion products and surface reaction mechanisms: a review, Mater. Corros. 66 (2015) 1206–1214.

[46] W.T. Bakker, The Effect of Chlorine on Mixed Oxidant Corrosion, in: D.A. Shores, R.A. Rapp, P.Y. Hou (Eds.), Proccedings Symp. Fundam. Asp. High Temp. Corros., The Electrochemical Society, San Antonio, Texas, 1996: pp. 241–255.

[47] B.P. Mohanty, D.A. Shores, Role of chlorides in hot corrosion of a cast Fe–Cr–Ni alloy. Part I: Experimental studies, Corros. Sci. 46 (2004) 2893–2907.

[48] N. Henriksen, M. Montgomery, O.H. Larsen, High Temperature Corrosion in Biomass-Fired Boilers, in: VDI-Conference, Deutscher Ingenieur-Verlag, 2002: pp. 111–133.

[49] S.C. Kung, High-Temperature Corrosion Mechanisms for Selected Iron and Nickel-Based Alloys Exposed to Sulfur and Chlorine-Containing Environments, Corrosion. 71 (2015) 483–501.

[50] W.J. Quadakkers, J. Żurek, M. Hänsel, Effect of water vapor on high-temperature oxidation of FeCr alloys, JOM. 61 (2009) 44–50.

[51] M. Nakai, Y. Murata, M. Morinaga, R. Hashizume, Effect of Impurity Sulfur on the Formation of Cr2O3 and SiO2 at the Early Stage of Steam Oxidation in both Ferittic and Austenitic Steels, Mater. Trans. 44 (2003) 1830–1838.

[52] H. Asteman, J.-E. Svensson, L.-G. Johansson, M. Norell, Indication of Chromium Oxide Hydroxide Evaporation During Oxidation of 304L at 873 K in the Presence of 10% Water Vapor, Oxid. Met. 52 (1999) 95–111.

[53] J. Pettersson, H. Asteman, J.-E. Svensson, L.-G. Johansson, KCl Induced Corrosion of a 304-type Austenitic Stainless Steel at 600°C; The Role of Potassium, Oxid. Met. 64 (2005) 23–41.

[54] A.N. Hansson, K. Pantleon, F.B. Grumsen, M.A.J. Somers, Microstructure Evolution During Steam Oxidation of a Nb Stabilized Austenitic Stainless Steel, Oxid. Met. 73 (2009) 289–309.

Supporting Information

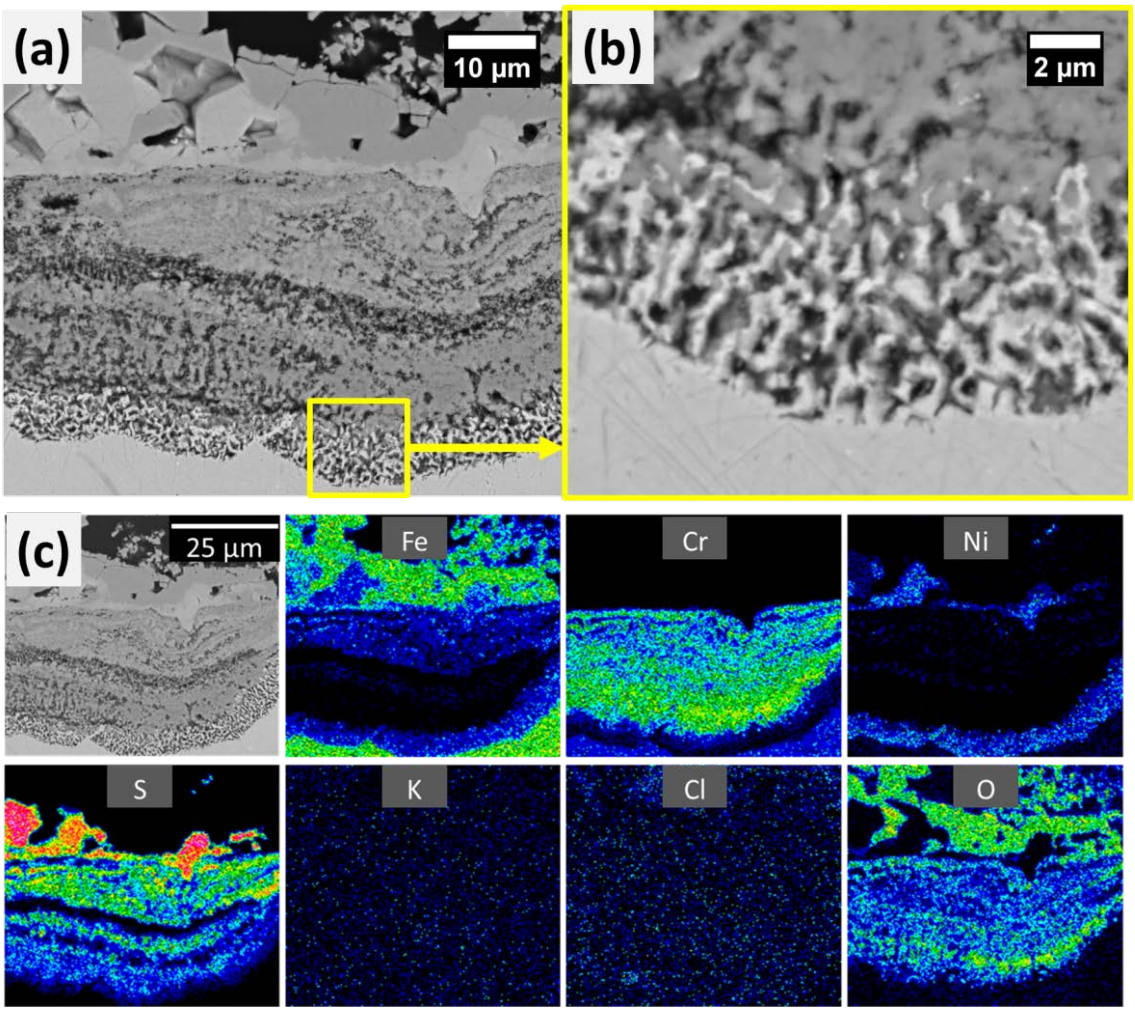

Figure S1. Microstructure (a and b) and composition (c) of pitting attack resulting from high temperature corrosion of TP 347H FG exposed to an oxidizing-sulphidizing gas mixture at 560 ºC for 72 h. The presence of a Ni-rich layer adjacent to the corrosion front is evident from the EDS maps in (c).